J. Fluid Mech. (1995), *vol.* 282, *pp.* 313–338

Instability of strained vortex layers and vortex tube formation in homogeneous turbulence

By T. PASSOT[1], H. POLITANO[1], P.L. SULEM[1], J.R. ANGILELLA[2] AND M. MENEGUZZI[3]†

[1] CNRS URA 1362, Observatoire de la Côte d'Azur, BP 229, 06304 Nice Cedex 4, France

[2] CERFACS, 42 Avenue G. Coriolis, 31057 Toulouse, France

[3] CERCA, 5160 Boulevard Décarie, Montreal, Quebec H2X 2H9, Canada

(Received 23 December 1993 and in revised form 20 June 1994)

A modulational perturbation analysis is presented which shows that when a strained vortex layer becomes unstable, vorticity concentrates into steady tubular structures with finite amplitude, in quantitative agreement with the numerical simulations of Lin & Corcos (1984). Elaborated three-dimensional visualizations suggest that this process, due to a combination of compression and self-induced rotation of the layer, is at the origin of intense and long-lived vortex tubes observed in direct numerical simulations of homogeneous turbulence.

1. Introduction

Numerical simulations of both stationary (Siggia 1981; Kerr 1985; Ashurst *et al.* 1987; She, Jackson & Orszag 1990, 1991; Ruetsch & Maxey 1991, 1992; Vincent & Meneguzzi 1991; Jiménez *et al.* 1993) and decaying homogeneous turbulence (Brachet 1991; Vincent & Meneguzzi 1994) reveal that regions of most intense vorticity appear as vortex tubes aligned with the eigenvector of the strain tensor associated with the intermediate eigenvalue. Their diameter is estimated as a few Kolmogorov scales or a fraction of the Taylor microscale, and their length can be comparable to the integral scale. They generally persist during many eddy-turnover times and are thus often referred to as coherent structures. They were recently detected in laboratory flows by noticing that vorticity concentrations produce local pressure minima (Douady, Couder & Brachet 1991). The aim of the present paper is to investigate the dynamical processes leading to the formation of such vortex tubes.

A detailed analysis of the early time dynamics of vortical ideal fluids with initial energy concentrated in large scales, was presented by Brachet *et al.* (1992). Numerical simulations by spectral methods in periodic geometry showed that in regions where it is strongly amplified, vorticity becomes aligned with the intermediate eigenvector of the strain tensor. Those regions take the form of pancakes (idealized as vortex layers) whose thickness rapidly decays in time. For a quantitative analysis, the minimal layer thickness is conveniently estimated by the width of the analyticity strip $\delta(t)$ of the velocity field. This quantity is given by half the logarithmic decrement of the energy spectrum, a quantity easily measured in the framework of spectral methods (Sulem, Sulem & Frisch 1983). One observes that after a short transient, $\delta(t)$

† On leave from CERFACS, 42 Avenue G. Coriolis, 31057 Toulouse, France

decays exponentially. This is consistent with the observation that the intermediate eigenvalue of the strain tensor, which is predominantly positive (Betchov 1956), remains bounded, while the two others diverge exponentially. This evolution proceeds until $\delta(t)$ becomes of the order of a few mesh sizes. Numerical accuracy is then lost. Persistence of an exponential decay during arbitrary long times would indicate well-posedness in the large for the three-dimensional Euler equation. Drastic changes could however occur if vortex layers formed at early times become unstable. This possible instability is however too slow to be observed in direct numerical simulations of inviscid flows without using spatial resolutions much beyond the possibilities of present day computers.

In §2, we address this question both in the context of viscous and inviscid flows, by deriving an asymptotic model for the dynamics of a strained vortex layer that leads to vorticity concentrations. In §3, we report on detailed visualizations showing the formation of vortex tubes in simulations of freely decaying homogeneous turbulence at resolutions up to $(256)^3$ collocation points and Reynolds numbers based on the integral scale up to 300. Comparisons with the main assumptions and predictions of the model are presented. Scaling properties of the vortex tubes together with their spectral signature in fully developed turbulence are also discussed. A brief summary of the main results is given in §4.

2. Dynamics of a strained vortex layer

In order to interpret the vorticity dynamics observed in direct numerical integrations of the Euler equations for boundary-free ideal flows, a local asymptotic analysis was presented by Brachet *et al.* (1992). It assumes that an initial vorticity blob shrinks in one direction (the z-direction), while in the other directions the typical scales remain of order unity. An approach analogous to an inner expansion for a boundary layer, leads to the conclusion that, owing to the incompressibility of the flow, both the layer shrinking and the vorticity growth should be exponential in time. Furthermore when arguing the sharp variations of the vorticity in the z-direction, variations in x and y are totally neglected and the vortex layer reduces to a unidimensional vorticity distribution

$$\Omega(x, y, z, t) = \mathrm{e}^{\gamma t} g(z\mathrm{e}^{\gamma t})\hat{e}_y \,, \tag{2.1}$$

subject to a uniform plane strain field

$$U(x, y, z, t) = \gamma y \hat{e}_y - \gamma z \hat{e}_z \,. \tag{2.2}$$

Here $\hat{e}_x$, $\hat{e}_y$, $\hat{e}_z$ denote unit vectors in the x-, y-, z-directions and γ a uniform rate of strain. The layer profile g is an arbitrary localized function. The streamwise velocity component associated with the layer reads $U_x(z, t) = f(z\mathrm{e}^{\gamma t})$ with $\mathrm{d}f/\mathrm{d}\xi = g(\xi)$. Equations (2.1) and (2.2) in fact provide an exact solution of the Euler equations. Since vorticity distribution (2.1) is uniform in the streamwise direction, it does not generate any self-induced advection. Vortex stretching is due to a uniform plane strain which can be viewed as locally modelling the action of external large-scale motions, and produces an indefinite shrinking of the layer thickness. In the same context, but in the presence of a (kinematic) viscosity ν, the problem admits a steady solution, the Burgers vortex layer whose thickness δ scales like $(\nu/\gamma)^{1/2}$ (Saffman 1992).

An important question concerns the stability of these strained vortex layers for both viscous and inviscid fluids, when subject to streamwise perturbations leading to a self-induced velocity. The stability of the (viscous) Burgers vortex layer was addressed

by Lin & Corcos (1984) in the context of free shear flows to explain the formation of streamwise vortices in the braid under the action of the strain due to adjacent spanwise rolls generated by the Kelvin–Helmholtz instability. Numerical integrations showed that a strained vortex layer may be unstable and that vorticity collapses into cylindrical vortices with circular cross-section. An asymptotic approach for long-wave perturbations (compared to the vortex thickness) was presented by Neu (1984), in the limit where the layer distortion is slaved to the vortex strength. Denoting by σ_0 the (unperturbed) circulation per unit length (vortex strength), the Burgers vortex layer appears to be unstable to infinitesimal perturbations when $\mu^2 \equiv \gamma\nu/\sigma_0^2 < \frac{1}{4}$. Special attention was devoted to the weakly nonlinear regime which is established slightly above the stability threshold. The resulting modulation equations admit stationary solutions corresponding to vorticity concentrations inside the vortex layer, but these solutions were shown to be unstable. A detailed analysis of the initial value problem is reported by Majda (1986) and Palais (1988) who proved that when the Burgers vortex layer is unstable, the modulation equations are well-posed only for a finite time during which vorticity concentrates. Afterwards a singularity occurs, which suggests that a more elaborated approach is required.

In this section, we reformulate the above modulation theory by getting rid of the assumption of slaved dynamics for the layer distortion and by including a variation of the layer thickness. We determine the linearly most unstable mode in precise agreement with the numerical integration of the Orr–Sommerfeld equation done by Lin & Corcos (1984). Furthermore, in the nonlinear regime, this approach leads to equations for which there is numerical evidence of well-posedness in the large and convergence to stationary solutions associated with vorticity concentrations. We also address the limit of zero strain and viscosity where the dynamics is governed by the Kelvin–Helmholtz instability, and the case of a strained vortex layer in an inviscid fluid.

2.1. *The asymptotic equations*

After a simple rescaling, we write the equation of motion of a vortex layer whose typical scale of variation L in the x-direction is large compared to its mean thickness $\delta_0 = \zeta L$, in the form

$$\zeta^2\omega_t + \zeta(u\omega)_x + ((w - \gamma z)\omega)_z = \nu(\zeta^2\partial_{xx}\omega + \partial_{zz}\omega)\,, \tag{2.3}$$

where $\omega = \omega(x, z, t)$ denotes the amplitude of the vorticity taken in the y-direction, and

$$u(x,z,t) = -\frac{\zeta}{2\pi}\int\int \frac{(z-z')\omega(x',z',t)}{(x-x')^2 + \zeta^2(z-z')^2}\mathrm{d}x'\mathrm{d}z', \tag{2.4}$$

$$w(x,z,t) = \frac{1}{2\pi}\int\int \frac{(x-x')\omega(x',z',t)}{(x-x')^2 + \zeta^2(z-z')^2}\mathrm{d}x'\mathrm{d}z' \tag{2.5}$$

are the components of the velocity field induced by the vortex layer.

In the limit of small ζ, the self-induced velocity can be expanded as

$$\begin{aligned}(x,z,t) = -\frac{1}{2}\int_{-\infty}^{+\infty} \mathrm{sgn}(z-z')\{&\omega(x,z',t) - \zeta|z-z'|\hat{\omega}_x(x,z',t)\\ &-\tfrac{1}{2}\zeta^2|z-z'|^2\omega_{xx}(x,z',t) + \ldots\}\mathrm{d}z',\end{aligned} \tag{2.6}$$

$$w(x,z,t) = \frac{1}{2}\int_{-\infty}^{+\infty} \{\hat{\omega}(x,z',t) + \zeta|z-z'|\omega_x(x,z',t) \\ -\tfrac{1}{2}\zeta^2(z-z')^2\hat{\omega}_{xx}(x,z',t) + ...\}\mathrm{d}z', \tag{2.7}$$

where

$$\hat{f}(x) = \frac{1}{2\pi}\int_{-\infty}^{+\infty} \frac{f(x')}{x-x'}\mathrm{d}x'$$

is the Hilbert transform of $f(x)$. Expansions (2.6), (2.7) were established by Neu (1984) using the two-dimensional character of the vortex layer and applying contour integration to the x'-variable. A direct proof is also possible. Although significantly longer, it easily extends to the fully three-dimensional situation where the layer is also modulated in the y-direction.

From the vortex strength

$$\sigma(x,t) = \int_{-\infty}^{+\infty} \omega(x,z,t)\mathrm{d}z \tag{2.8}$$

and the two first vorticity momenta,

$$\chi(x,t) = \int_{-\infty}^{+\infty} z\omega(x,z,t)\mathrm{d}z, \tag{2.9}$$

$$\alpha(x,t) = \int_{-\infty}^{+\infty} z^2\omega(x,z,t)\mathrm{d}z, \ , \tag{2.10}$$

we reconstruct the local distortion of the layer

$$\eta(x,t) = \frac{\chi(x,t)}{\sigma(x,t)} \tag{2.11}$$

and its local thickness

$$\delta(x,t) = \frac{1}{\sigma}\left(\int_{-\infty}^{+\infty}(z-\eta(x,t))^2\omega(x,z,t)\mathrm{d}z\right)^{1/2} \\ = \left(\frac{\alpha}{\sigma} - \left(\frac{\chi}{\sigma}\right)^2\right)^{1/2}, \tag{2.12}$$

which together with σ can be viewed as 'collective coordinates' of the vortex layer.

Substituting (2.6)–(2.7) into (2.3), multiplying by $(1, z, z^2)$ and integrating on z, we obtain

$$\sigma_t = \nu\sigma_{xx} - \tfrac{1}{2}(\chi\hat{\sigma}_x - \hat{\chi}_x\sigma)_x + O(\zeta), \tag{2.13}$$

$$\zeta^2\chi_t = -\gamma\chi + \tfrac{1}{2}\sigma\hat{\sigma} + O(\zeta), \tag{2.14}$$

$$\zeta^2\alpha_t = -2\gamma\alpha + \chi\hat{\sigma} + 2\nu\sigma + O(\zeta)\ . \tag{2.15}$$

This is a closed system for σ, χ and α which evolves on two timescales. The long timescale gives the evolution of the strength σ. The short one corresponds to the early exponential shrinking of an inviscid layer. Note that at this order of approximation, the non-zero thickness of the vortex layer does not affect the collective dynamics.

When the layer deformation is assumed to be slaved to the vortex strength, (2.14) reduces to

$$\chi = \frac{1}{2\gamma}\sigma\hat{\sigma}\ , \tag{2.16}$$

and the nonlinear term in (2.13) becomes

$$(\chi\hat{\sigma}_x - \hat{\chi}_x\sigma)_x = \frac{1}{\gamma}\{\sigma[\tfrac{1}{2}(\hat{\sigma})^2 - \sigma\hat{\sigma}]_x\}_x$$
$$= \frac{1}{2\gamma}(\sigma^2\sigma_x)_x \,, \tag{2.17}$$

where the last identity is proved in Appendix C of Neu (1984). We thus recover the nonlinear backward heat equation (5.5) of Neu (1984) which is usually ill-posed.

At the level of (2.13)–(2.15), the existence problem remains open. Nevertheless, linearization about a layer of strength σ_0 leads to a dispersion relation for an harmonic perturbation $e^{\lambda t+ikx}$, of the form

$$\zeta^2\lambda^2 + (\gamma + \zeta^2\nu k^2)\lambda + \sigma_0^2\left(\frac{\gamma\nu}{\sigma_0^2} - \frac{1}{4}\right)k^2 = 0 \,. \tag{2.18}$$

In the long-wave limit ($\zeta k \ll 1$), the growth rate scales like the square wavenumber, as in the slaved approximation. Short-wave disturbances however do not feel the strain: at zero viscosity, the growth rate varies like the wavenumber, as in the usual Kelvin–Helmholtz instability.

Viscosity is not sufficient to ensure small-scale regularization. In contrast, a finite thickness for the vortex layer suppresses the Kelvin–Helmholtz instability for perturbations whose wavelength is smaller than a critical value which is of the order of the layer thickness and depends on the vorticity profile (Chandrasekhar 1961). In order to capture this effect, it is necessary to estimate the $O(\zeta)$-terms denoted F_1, F_2 and F_3 in (2.13)–(2.15) respectively. They read

$$F_1 = \frac{\zeta}{4}\int\int \mathrm{sgn}(z-z')(z-z')^2\omega_{xx}(x,z')\omega(x,z)\mathrm{d}z\mathrm{d}z'$$
$$= \frac{\zeta}{4}\partial_x\int\int \mathrm{sgn}(z-z')(z-z')^2\omega_x(x,z')\omega(x,z)\mathrm{d}z\mathrm{d}z' \,, \tag{2.19}$$

$$F_2 = \frac{\zeta}{2}\partial_x\int\int z(z-z')\omega(x,z')\omega(x,z)\mathrm{d}z\mathrm{d}z'$$
$$+\frac{\zeta}{2}\int\int |z-z'|\omega_x(x,z')\omega(x,z)\mathrm{d}z\mathrm{d}z' \,, \tag{2.20}$$

$$F_3 = -\frac{\zeta}{2}\int\int z|z-z'|\omega_x(x,z')\omega(x,z)\mathrm{d}z\mathrm{d}z'$$
$$-\frac{\zeta}{4}\int\int \mathrm{sgn}(z-z')(z-z')^2\omega_x(x,z')\omega(x,z)\mathrm{d}z\mathrm{d}z' \,. \tag{2.21}$$

In general, these integrals cannot be expressed in an exact closed form in terms of σ, χ and α. To estimate them, we expand the vorticity field in the form

$$\omega(x,z,t) = \omega^{(0)}(x,z,t) + \zeta\omega^{(1)}(x,z,t) + \cdots \,, \tag{2.22}$$

with similar expansions for the collective coordinates. We write $\omega^{(0)}$ as a modulation of a uniform vortex layer, in the form

$$\omega^{(0)}(x,z,t) = \frac{\sigma^{(0)}(x,t)}{\delta^{(0)}(x,t)}g\left(\frac{z-\eta^{(0)}(x,t)}{\delta^{(0)}(x,t)}\right) \,. \tag{2.23}$$

At early times or in the inviscid limit, the function g is determined by the initial conditions, while after the layer thickness has saturated due to viscosity, it is given

by the profile

$$g(z) = \frac{1}{(2\pi)^{1/2}} e^{-z^2/2} \tag{2.24}$$

of the Burgers vortex layer.

Computing ω_x and substituting in (2.19)–(2.21), we obtain

$$F_1 = -\zeta\{J_1(\sigma\chi_x - \chi\sigma_x)\delta + J_2\sigma^2\delta\delta_x\}_{xx} + O(\zeta^2)\,, \tag{2.25}$$

$$F_2 = \zeta\{J_1(\sigma^2)_x\delta - (\tfrac{1}{2}J_1 + J_3)\sigma^2\delta_x\} + O(\zeta^2)\,, \tag{2.26}$$

$$F_3 = -\zeta J_4(\sigma\chi_x - \sigma_x\chi)\delta - \zeta J_5\sigma^2\delta^3 + O(\zeta^2)\,, \tag{2.27}$$

where, consistently with the order of the approximation, we replaced the leading terms of the collective coordinates by these coordinates themselves. The numerical coefficients J_1, J_2, J_3, and J_4 are expressed in terms of the layer profile by

$$J_1 = \frac{1}{4}\int\int \mathrm{sgn}(\xi - \xi')(\xi - \xi')^2 g(\xi)\frac{\mathrm{d}g}{\mathrm{d}\xi'}(\xi')\mathrm{d}\xi\mathrm{d}\xi'$$

$$= \frac{1}{2}\int\int |\xi - \xi'| g(\xi)g(\xi')\mathrm{d}\xi\mathrm{d}\xi'\,, \tag{2.28}$$

$$J_2 = \frac{1}{4}\int\int \mathrm{sgn}(\xi - \xi')(\xi - \xi')^2 g(\xi)\xi'\frac{\mathrm{d}g}{\mathrm{d}\xi'}(\xi')\mathrm{d}\xi\mathrm{d}\xi'\,, \tag{2.29}$$

$$J_3 = \frac{1}{2}\int\int |\xi - \xi'|\frac{\mathrm{d}g}{\mathrm{d}\xi'}(\xi')g(\xi)\mathrm{d}\xi\mathrm{d}\xi' = \frac{1}{2}J_1\,, \tag{2.30}$$

$$J_4 = \frac{1}{2}\int\int \mathrm{sgn}(\xi - \xi')(\xi - \xi')^2 g(\xi)\frac{\mathrm{d}g}{\mathrm{d}\xi'}(\xi')\mathrm{d}\xi\mathrm{d}\xi' = -2J_1\,, \tag{2.31}$$

$$J_5 = \int\int \xi'|\xi - \xi' g(\xi)\frac{\mathrm{d}g}{\mathrm{d}\xi'}(\xi')\mathrm{d}\xi\mathrm{d}\xi'\,. \tag{2.32}$$

Assuming that the layer profile is symmetric ($g(\xi) = g(-\xi)$), we have $J_2 = J_5 = 0$. The only remaining coefficient is J_1. For the Burgers vortex layer, $J_1 = 1/\pi^{1/2}$.

At this step, it is convenient to rewrite the dynamic equations using dimensionless variables. Let σ_0 denote the typical value of the vortex strength. Using the perturbation scale L as the unit length and L/σ_0 as the unit time, and measuring σ, χ, α and δ in units of σ_0, $\sigma_0 L$, $\sigma_0 L^2$ and L respectively, we obtain

$$\sigma_t = \frac{1}{R}\sigma_{xx} - \tfrac{1}{2}(\chi\hat{\sigma}_x - \hat{\chi}_x\sigma)_x - \frac{\zeta}{\pi^{1/2}}\{(\sigma\chi_x - \chi\sigma_x)\delta\}_{xx}\,, \tag{2.33}$$

$$\zeta^2\chi_t = -S\chi + \tfrac{1}{2}\sigma\hat{\sigma} + \frac{\zeta}{\pi^{1/2}}\{(\sigma^2)_x\delta - \sigma^2\delta_x\}\,, \tag{2.34}$$

$$\zeta^2\alpha_t = -2S\alpha + \chi\hat{\sigma} + \frac{2}{R}\sigma + \frac{2\zeta}{\pi^{1/2}}(\sigma\chi_x - \sigma_x\chi)\delta\,, \tag{2.35}$$

where δ is given by (2.12). The parameters $R = L\sigma_0/\nu$ and $S = \gamma L/\sigma_0$ respectively denote the Reynolds number at the scale of the layer perturbation and the ratio of this scale to the internal scale σ_0/γ. In these units, δ and α are initially of order ζ and ζ^2 respectively, while σ and χ are of order unity.

Except when the strain or the viscosity are asymptotically small, we can rewrite (2.33)–(2.35) with only two parameters $\epsilon = \zeta/S$ and $\mu = (S/R)^{1/2}$, by rescaling $t = S\tilde{t}$, $\chi = (1/S)\tilde{\chi}$, $\alpha = (1/SR)\tilde{\alpha}$, $\delta = (SR)^{-1/2}\tilde{\delta}$. We get (after dropping the tilde symbol)

$$\sigma_t = \mu^2\sigma_{xx} - \tfrac{1}{2}(\chi\hat{\sigma}_x - \hat{\chi}_x\sigma)_x - \frac{\epsilon\mu}{\pi^{1/2}}\{(\sigma\chi_x - \chi\sigma_x)\delta\}_{xx}\,, \tag{2.36}$$

$$\epsilon^2\chi_t = -\chi + \tfrac{1}{2}\sigma\hat{\sigma} + \frac{\epsilon\mu}{\pi^{1/2}}\{(\sigma^2)_x\delta - \sigma^2\delta_x\}\ , \tag{2.37}$$

$$\epsilon^2\alpha_t = -2\alpha + \frac{1}{\mu^2}\chi\hat{\sigma} + 2\sigma + \frac{2}{\pi^{1/2}}\frac{\epsilon}{\mu}(\sigma\chi_x - \sigma_x\chi)\delta\ , \tag{2.38}$$

where

$$\delta = \left(\frac{\alpha}{\sigma} - \frac{1}{\mu^2}\left(\frac{\chi}{\sigma}\right)^2\right)^{1/2}\ . \tag{2.39}$$

The parameter

$$\mu = (\nu\gamma/\sigma_0^2)^{1/2} \tag{2.40}$$

can be viewed as the inverse Reynolds number at the internal scale. Choosing the mean layer thickness $\delta_0 = (\nu/\gamma)^{1/2}$, like in the (unperturbed) Burgers vortex layer, we get

$$\epsilon = \frac{\mu}{S^2}\ . \tag{2.41}$$

When, in the limit $\epsilon \ll 1$, the layer distortion is slaved to the vortex strength, we recover equation (6.22) of Neu (1984), up to the value of a numerical coefficient in the $O(\epsilon)$-term. In fact, the order of magnitude of ϵ can be chosen at will, the asymptotics only requiring that

$$\zeta = \epsilon S = \mu/S = (SR)^{-1/2} = (\epsilon\mu)^{1/2} \ll 1\ . \tag{2.42}$$

2.2. *Linear stability analysis*

Linearizing (2.36)–(2.39) about the solution corresponding to the Burgers vortex by taking $\sigma = 1 + s$ and $\alpha = 1 + a$ with $s, \chi, a \ll 1$, we get

$$s_t = \tfrac{1}{2}\hat{\chi}_{xx} + \mu^2 s_{xx} - \frac{\epsilon\mu}{\pi^{1/2}}\chi_{xxx}\ , \tag{2.43}$$

$$\epsilon^2\chi_t = -\chi + \tfrac{1}{2}\hat{s} + \frac{\epsilon\mu}{\pi^{1/2}}\{\tfrac{5}{2}s_x - \tfrac{1}{2}a_x\}\ , \tag{2.44}$$

$$\epsilon^2 a_t = -2a + 2s + \frac{2\epsilon}{\mu\pi^{1/2}}\chi_x\ . \tag{2.45}$$

The dispersion relation for a perturbation $e^{\lambda t + ikx}$ is conveniently written in terms of the variables $\Lambda = \epsilon^2\lambda$ and $\kappa = \epsilon k$, in the form

$$\Lambda^3 + (3 + \mu^2\kappa^2)\Lambda^2 + \Lambda\left\{2 - \left(\frac{1}{\pi} + \frac{1}{4} - 3\mu^2\right)\kappa^2 + \frac{3\mu}{4\pi^{1/2}}|\kappa|^3 + \frac{5}{2}\frac{\mu^2}{\pi}\kappa^4\right\} + (2\mu^2 - \tfrac{1}{2})\kappa^2 + \frac{\mu}{\pi^{1/2}}|\kappa|^3 + \frac{3\mu^2}{\pi}\kappa^4 = 0 \tag{2.46}$$

which depends only on μ. Figure 1 displays the real part of the three eigenvalues versus κ for $\mu = 0.25$. In the long-wave limit ($\kappa \ll 1$), we recover from (2.46) the same growth rate $\Lambda = (\frac{1}{4} - \mu^2)\kappa^2$, as in the slaved approximation for the leading eigenvalue, but also the two other solutions -1 and -2, associated with damped eigenmodes. In the short-wave limit ($\kappa \gg 1$), (2.46) reduces to

$$\Lambda^3 + \mu^2\kappa^2\Lambda^2 + \frac{5}{2}\frac{\mu^2}{\pi}\kappa^4\Lambda + \frac{3\mu^2}{\pi}\kappa^4 = 0\ . \tag{2.47}$$

The three eigenvalues have the asymptotic form

$$\Lambda_0 = -\tfrac{6}{5}\ , \qquad \Lambda_\pm = -\frac{\mu^2\kappa^2}{2}\left\{1 \pm \mathrm{i}\left(\frac{10}{\pi\mu^2} - 1\right)^{1/2}\right\}\ . \tag{2.48}$$

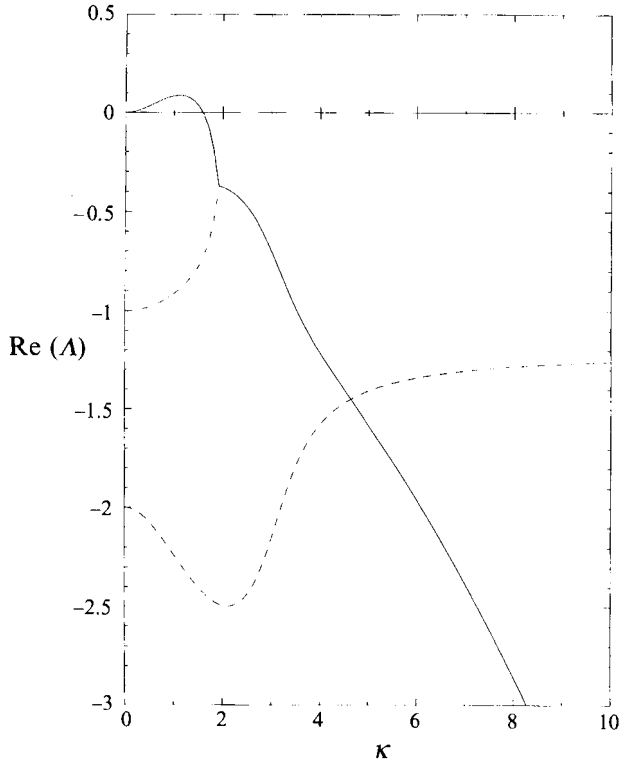

FIGURE 1. Real part of the three eigenvalues Re(Λ) versus κ for $\mu = 0.25$.

Coming back to the dimensional variables $\tilde{\Lambda} = \gamma\Lambda$ and $K = (\gamma/\sigma_0)\kappa$, (2.48) reads

$$\tilde{\Lambda}_0 = -\tfrac{6}{5}\gamma\,, \qquad \tilde{\Lambda}_\pm = -\frac{K^2}{2}\left\{\nu \pm \mathrm{i}\left(\frac{10}{\pi}\frac{\sigma_0^2\gamma}{\nu} - \nu^2\right)^{1/2}\right\}\,. \tag{2.49}$$

In the limit $\gamma \to 0$, $\nu \to 0$, with the condition that the layer thickness $\delta_0 = (\nu/\gamma)^{1/2}$ remains finite, we get

$$\tilde{\Lambda}_\pm = \mathrm{i}(5/2\pi)^{1/2}\frac{|\sigma_0|}{\delta_0}K^2\,, \tag{2.50}$$

which reproduces the oscillatory behaviour of short-wavelength perturbations of an unstrained inviscid vortex layer with finite thickness (Chandrasekhar 1961).

In the limit of small μ, it is convenient to measure the disturbance wavelength and the layer thickness with the same unit by defining $q = \mu\kappa$. The associated growth rate is also rescaled as $p = \mu\Lambda$. In these units, the growth rate of one of the eigenmodes tends to zero with μ, while the two others remain finite. They are displayed in figure 2 for $\mu = 0.005$. The three eigenvalues can easily be computed asymptotically. Two special points deserve extra attention: (i) one of the eigenmodes which was damped at small wavenumber becomes unstable for $q > 0.486$, (ii) when real, the dominant mode satisfies

$$p^2 \approx \left(\frac{1}{\pi} + \frac{1}{4}\right)q^2 - \frac{3}{4\pi^{1/2}}|q|^3 - \frac{5}{2\pi}q^4\,. \tag{2.51}$$

The most unstable mode is thus given by $q_M = 0.43$ and corresponds to a growth rate

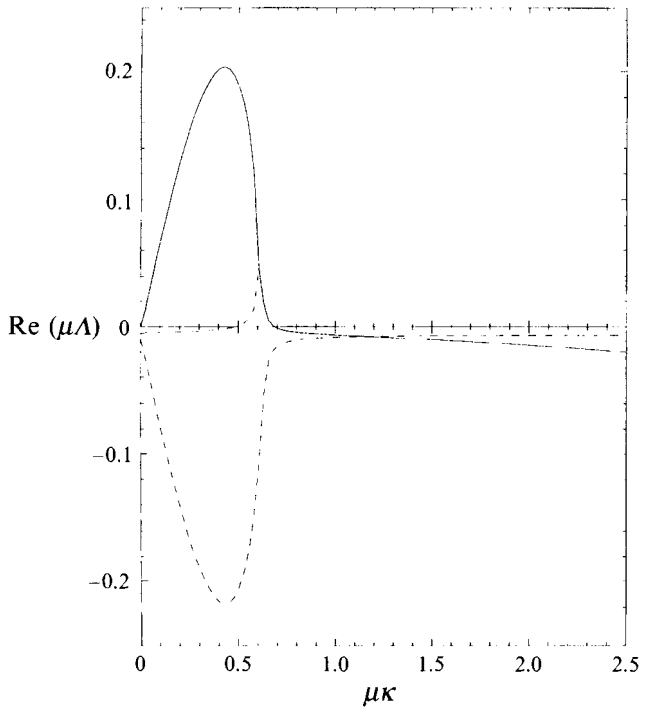

FIGURE 2. Real part of the three rescaled eigenvalues Re(p) versus q for $\mu = 0.005$.

$p_M = 0.21$, in excellent agreement with the numerical solution of the Orr–Sommerfeld equation given in figure 16 of Lin & Corcos (1984). The associated perturbation wavelength exceeds the layer thickness by a factor of order 15, which validates the asymptotics and explains the agreement with the direct linear analysis. The eigenmode $(\sigma_e, \chi_e, \alpha_e)$ scales like $(1/\mu, 1, 1/\mu)$ or like $(\zeta^{-1}, 1, \zeta)$ when coming back to the physical variables, which corresponds to a strong dominance of the vorticity concentration on the layer distortion.

As noted by Lin & Corcos (1984), a significant difference is obtained when the layer distortion is assumed to be slaved (Neu 1984). In this case, the growth rate is $\Lambda = \kappa^2(\frac{1}{4} - \mu^2) - (\mu/2\pi^{1/2})|\kappa|^3$. In the limit $\mu \to 0$ the most unstable mode $q_M = \mu k_M = \pi^{1/2}/3$ has a growth rate $p_M = \mu\Lambda_M = (\pi/108)/\mu$ which increases linearly with the Reynolds number, instead of saturating at a finite value.

2.3. *The nonlinear dynamics*

In order to investigate the nonlinear dynamics described by (2.36)–(2.39), we have integrated these equations in a periodic domain using a Fourier spectral method in space and a finite difference scheme for the time stepping. A resolution of 128 collocation points was retained. When the nonlinear terms are treated by a completely explicit scheme, numerical stability prescribes sharp constraints on the time step. Indeed, a weakly nonlinear analysis of (2.36)–(2.39) in the slaved limit shows the presence of a fourth-order dissipative term $\epsilon^2\sigma_{xxxx}$, in addition to the third-order regularizing term $\epsilon\sigma_{xxx}$ retained in equation (7.1) of Neu (1984). In order to relax the most stringent condition on the time step, we resorted to using a semi-implicit scheme where terms $c\sigma_{xxxx}$, $c\chi_{xxxx}$ and $c\alpha_{xxxx}$ are added and subtracted in (2.36)–(2.38) respectively. The stabilizing terms are handled implicitly by a Crank–

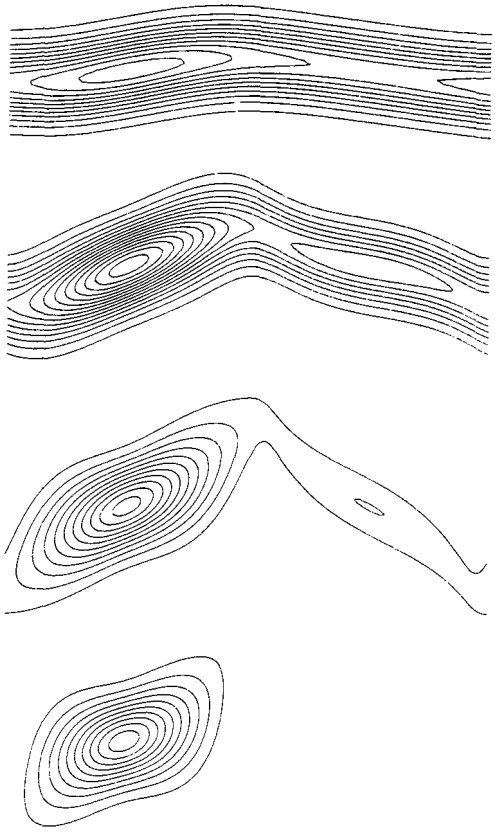

FIGURE 3. Vorticity field for the asymptotic model of §2 with $\epsilon = 0.5$ and $\mu = 0.32$, at times (from top to bottom) $t = 5$ (contours from 0 to 1.1 by intervals of 0.1), $t = 15$ (contours from 0 to 1.5 by intervals of 0.1, $t = 25$ (contours from 0 to 2.2 by intervals of 0.2) and $t = 100$ (contours from 0 to 3 by intervals of 0.3).

Nicholson scheme, while the unstable ones, together with all the other terms of the equations are treated by an explicit third-order Runge–Kutta scheme. This scheme, suggested by analysing the slaved limit, allows a significant gain (up to a factor 10) on the time step when solving the full system (2.36)–(2.39).

Fixing the computational domain to be 2π-periodic, we took the same initial data $\sigma(x,0) = 1 + 0.1 \sin k_0 x$, $\chi(x,0) = \frac{1}{2}\sigma(x,0)\hat{\sigma}(x,0)$, $\alpha(x,0) = 1$, and varied μ and ϵ. This choice of $\alpha(x,0)$ (and thus of $\delta(x,0)$) suppresses a possible exponential shrinking of the layer thickness, obtained at early time when $\delta(x,0)$ is significantly larger than its mean equilibrium value. Except when explicitly mentioned, we used $k_0 = 1$.

A main observation is that, in contrast with the slaved limit studied by Neu (1984), Majda (1986) and Palais (1988), solutions of (2.36)–(2.39) do not blow up in a finite time but relax to a steady state. This is illustrated in figures 3 and 4, obtained for $\epsilon = 0.5$ and $\mu = 0.32$. Figure 3 shows vorticity contours at times $t = 5$, 15 , 25 and 100 when the asymptotic steady state has been reached. The contours are obtained by reconstructing the vortex layer from the collective coordinates σ, η, δ using (2.23)–(2.24). The distortion of the initial vortex layer and the vorticity concentration into a vortex tube satisfactorily reproduces the results of direct numerical integration of (2.3), presented by Lin & Corcos (1984). Figure 4 gives the profiles of the collective

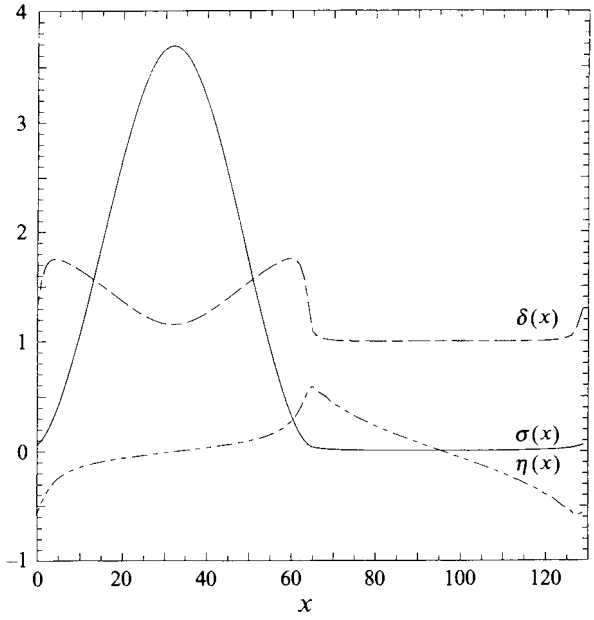

FIGURE 4. Steady state for the vortex strength $\sigma(x)$, the layer deformation $\eta(x)$ and the layer thickness $\delta(x)$ for the same conditions as in figure 3, reached at $t = 100$.

coordinates at the final time (the x-axis is labelled by grid points). In order to observe the influence of the parameter μ, we also performed a run with $\epsilon = 0.5$ and $\mu = 0.25$. In addition to the main vorticity concentration, a weaker peak appears and amplifies for a while, after which it tends to relax. Figure 5(a) shows the profiles of σ , η and δ close to the time when the secondary peak reaches its maximum, while figure 5(b) displays the same quantities at the latest time of the simulation. Later on, gradients become too sharp for the resolution we used. The experience we got from other simulations nevertheless suggests that a simple structure with large gradients will eventually emerge. Stable solutions displaying several maxima may however exist. An example was obtained numerically for $k_0 = 3$ with $\mu = 0.2$ and $\epsilon = 0.5$. It follows that the steady state reached for given values of ϵ and μ may depend on the initial conditions. The competition between vorticity structures with the same sign often leads (although not necessarily) to the emergence of a single tube.

Several vorticity concentrations may also develop when decreasing the value of ϵ. We performed a simulation with $\mu = 0.32$ and $\epsilon = 0.1$. Figure 6 shows vorticity contours at times $t = 1$, 2.5, 2.8 and 3.3, while figure 7 displays the profiles of σ, η and δ at the final time ($t = 3.3$) of the computation. During the period of integration, several vorticity concentrations are visible. At the latest time, secondary peaks are still growing. However, owing to the formation of very sharp gradients, the integration cannot be carried over longer times without a dramatic increase of space and time resolutions. A comprehensive parametric study of (2.36)–(2.39), although feasible, would be very costly without the development of specific algorithms able to cope with the stiffness of the asymptotic equations. The present results nevertheless clearly display vorticity concentrations within strained vortex layers and the formation of vortex tubes.

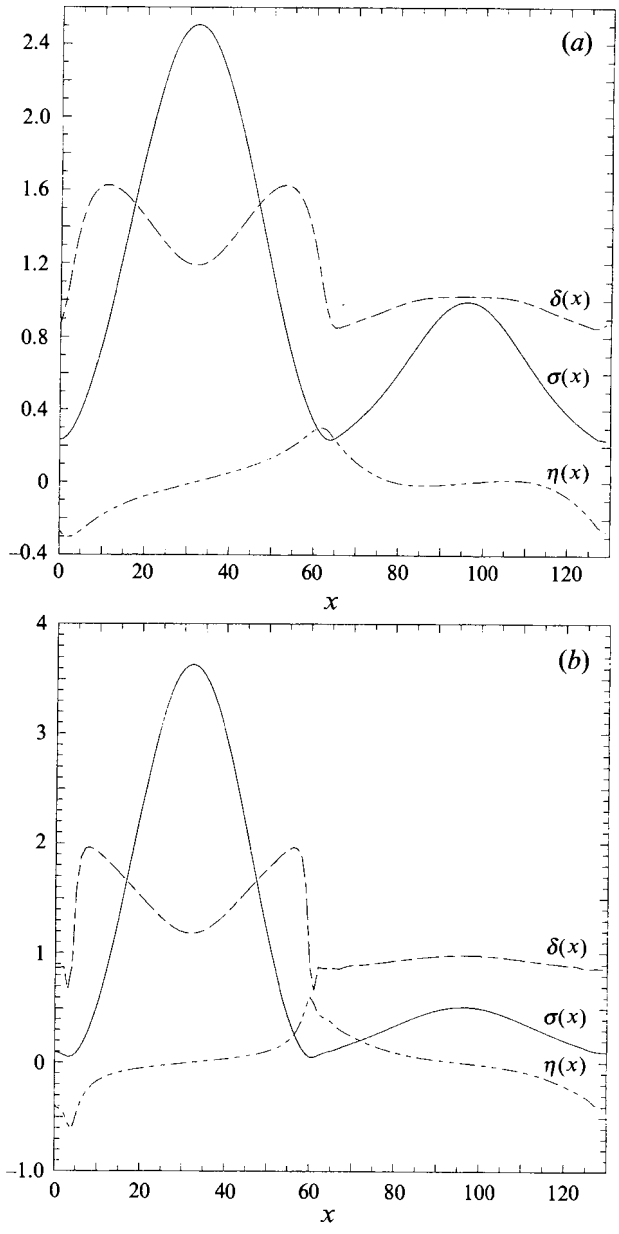

FIGURE 5. Vortex strength $\sigma(x)$, layer deformation $\eta(x)$ and layer thickness $\delta(x)$ for $\epsilon = 0.5$ and $\mu = 0.25$: (*a*) at a time $t = 12$ close to the maximum intensity of the secondary vorticity concentration; (*b*) at the latest time $t = 21$ of the simulation.

2.4. *The limit of zero strain and viscosity*

In the formulation (2.33)–(2.35), the collective coordinate formalism also enables us to address the limit of vanishing strain and viscosity where the layer dynamics is governed by the self-distorsion induced by the Kelvin–Helmholtz instability. In the framework of long-wave asymptotics, the limit $S \to 0$ also requires $R \to \infty$ in order to preserve the condition $\zeta = (RS)^{-1/2} \ll 1$.

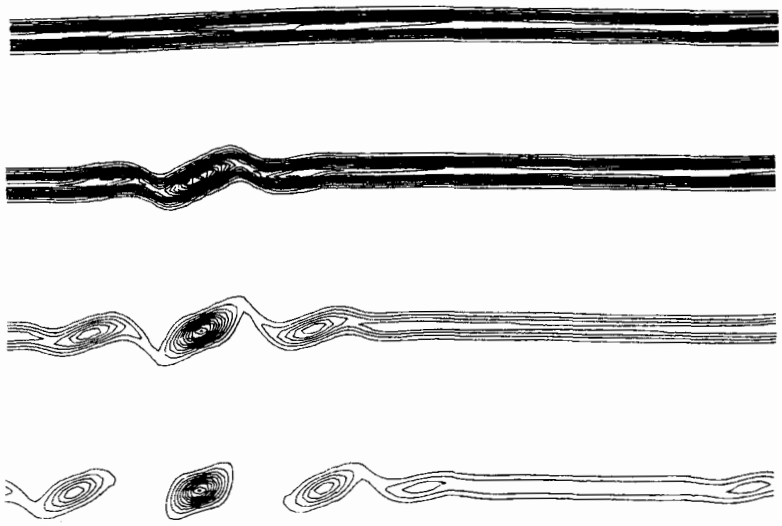

FIGURE 6. Vorticity contours for the asymptotic model with $\epsilon = 0.1$ and $\mu = 0.32$ at times (from top to bottom) $t = 1$ (contours from 0 to 1.1 by intervals of 0.1), $t = 2.5$ (contours from 0 to 1.6 by intervals of 0.1), $t = 2.8$ (contours from 0 to 2.4 by intervals of 0.2) and $t = 3.3$ (contours from 0 to 3.3 by intervals of 0.3).

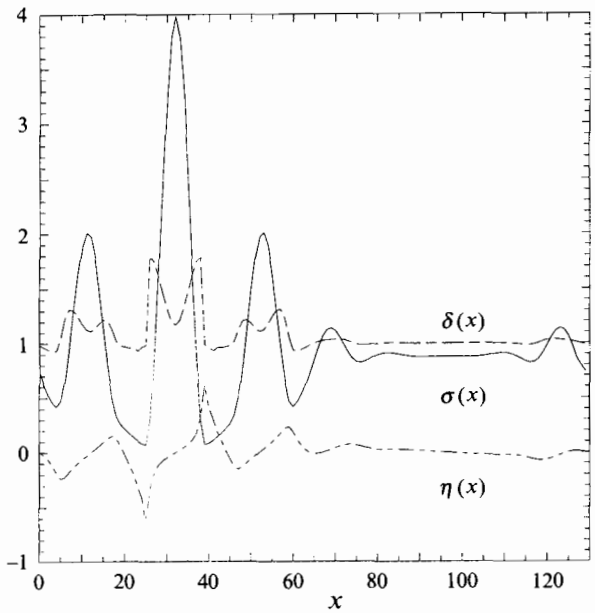

FIGURE 7. Vortex strength $\sigma(x)$, layer deformation $\eta(x)$ and layer thickness $\delta(x)$ at the latest time $t = 3.3$ of the simulation for the same run as in figure. 6.

A numerical integration was performed with the initial conditions $\sigma = 1+0.01 \sin x$, $\chi = 0$ and $\delta = 1$. This prescribes $\zeta = \delta_0/L = 1/2\pi \approx 0.16$. Figure 8 shows the collective coordinates at the latest reliable time $t = 0.9$ of the simulation. The layer distorsion is clearly the dominant process in contrast with the case where S is of order unity. Figure 9 which shows the layer deformation versus the circulation

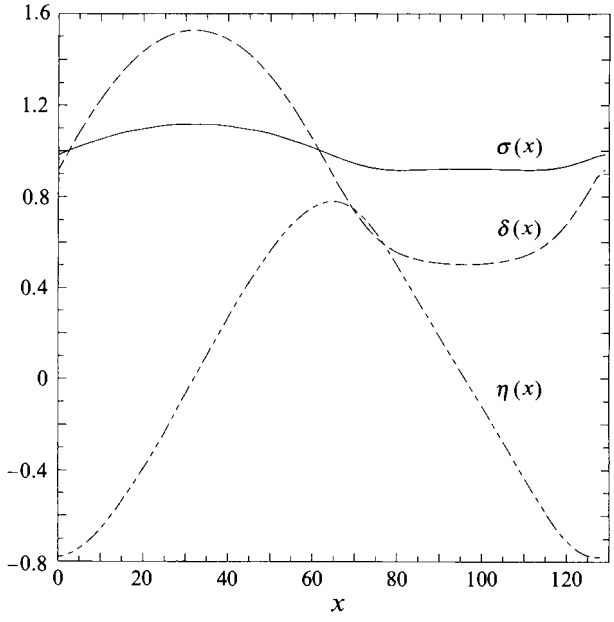

FIGURE 8. Vortex strength $\sigma(x)$, layer deformation $\eta(x)$ and layer thickness $\delta(x)$ for $S = 0$, $R = \infty$, $\zeta = 0.16$ at $t = 0.9$

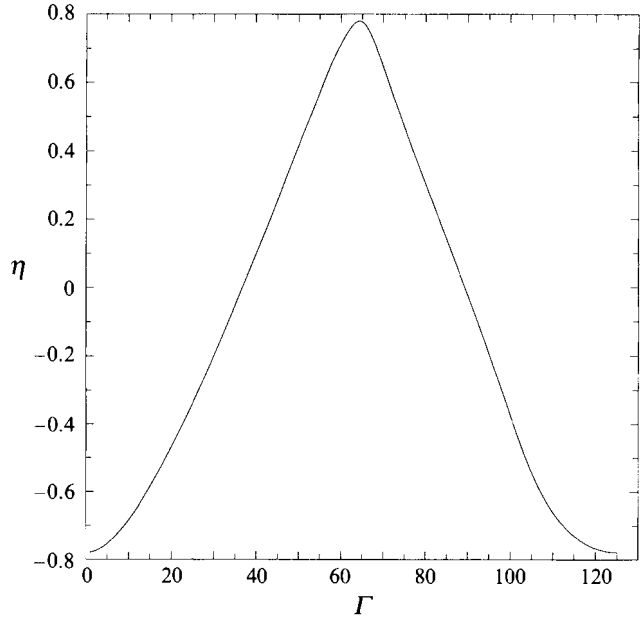

FIGURE 9. Layer deformation versus the circulation Γ for the same situation as figure 8.

$\Gamma(x,t) = \int_0^x \sigma(x',t)\mathrm{d}x'$, illustrates the tendency to form a cusp singularity in the limit of an infinitely thin layer, (Meiron, Baker & Orszag 1982). The later evolution, as observed e.g. by Baker & Shelley (1990), is outside the scope of the present formalism.

2.5. *The dynamics of a strained vortex in the inviscid limit*

The equations of motion are given by (2.33)–(2.35) with $1/R = 0$. In this regime, a dominant effect is the exponential shrinking of the layer thickness, which limits the numerical integration to short times. The difficulty is however easily overcome by using a time-dependent rescaling in the form $\xi = e^{St}x$, $\tau = (e^{St} - 1)/S$, together with $\sigma(x,t) = \Sigma(\xi,\tau)$, $\chi(x,t) = e^{-St}X(\xi,\tau)$, $\alpha(x,t) = e^{-2St}A(\xi,\tau)$, $\delta(x,t) = e^{-St}\Delta(\xi,\tau)$. The equations become

$$\Sigma_\tau + \frac{S}{1+S\tau}\xi\frac{\partial\Sigma}{\partial\xi} = -\tfrac{1}{2}(X\hat{\Sigma}_\xi - \hat{X}_\xi\Sigma)_\xi - J_1\zeta\{(\Sigma X_\xi - X\Sigma_\xi)\Delta\}_{\xi\xi}\,, \quad (2.52)$$

$$\zeta^2\left(X_\tau + \frac{S}{1+S\tau}\xi\frac{\partial X}{\partial\xi}\right) = \tfrac{1}{2}\Sigma\hat{\Sigma} + J_1\zeta\{(\Sigma^2)_\xi\Delta - \Sigma^2\Delta_{xi}\}\,, \quad (2.53)$$

$$\zeta^2\left(A_\tau + \frac{S}{1+S\tau}\xi\frac{\partial A}{\partial\xi}\right) = X\hat{\Sigma} + 2J_1\zeta(\Sigma X_\xi - \Sigma_\xi X)\Delta\,, \quad (2.54)$$

where the parameter J_1 is defined in (2.28) and depends on the initial profile g of the vortex layer. Providing the second term on the left-hand side becomes negligible for long enough times, we recover the system studied in §2.4 up to the time-dependent rescaling of the variables. When coming back to the primitive variables, the amplitude of the layer deformation is strongly reduced. Furthermore, the scale of the perturbation in the x-direction and the layer thickness display similar scalings in time. It follows that the aspect ratio of the vortex structure is preserved and that the formation of quasi-circular tubes is not expected. This leads one to conclude that viscosity is an essential ingredient in the scenario of tube formation discussed in this paper.

3. Vortex tubes in homogeneous turbulence

3.1. *Visualization of vortex tubes in direct numerical simulations*

In this section we analyse the development of intense vorticity structures in a numerical integration of the Naviers–Stokes equations for decaying turbulence. Periodic boundary conditions are assumed and a pseudo-spectral method with a resolution of $(256)^3$ grid points is used. Random initial conditions with an energy spectrum (defined by averaging half the square Fourier transform of the velocity field on a spectral shell of unit width around the sphere of radius k) $E_0(k) = 0.03k^2e^{-(k/k_0)^2}$ peaked at the wavenumber $k_0 = 1$, are chosen. They are the same as those used in one of the inviscid simulations presented in Brachet *et al.* (1992). The initial Reynolds number $Re = u_0l_0/\nu$ is approximately 300. Here the r.m.s. velocity u_0 is defined as $u_0^2 = \frac{2}{3}\int E(k)\mathrm{d}k \approx 0.04$, the integral scale as $l_0 = (\pi/2u_0^2)\int k^{-1}E(k)\mathrm{d}k \approx 1.5$, and the viscosity is $\nu = 10^{-3}$.

Figure 10 provides the main characteristic times of the run by displaying the temporal evolution of (*a*) the total energy $E(t)$, (*b*) the enstrophy (mean square vorticity) $\Omega(t)$, together with (*c*) the logarithmic decrement $\delta(t)$ and (*d*) the algebraic prefactor $n(t)$ obtained by fitting at each instant of time, the computed energy spectrum by a function of the form $c(t)k^{n(t)}e^{-2\delta(t)k}$. In order to check the stability of the fit, three ranges of wavenumbers $5 \leqslant k \leqslant 107$, $5 \leqslant k \leqslant 117$ and $5 \leqslant k \leqslant 127$ are considered. At the time $t \approx 10.5$ when the enstrophy and thus the energy dissipation reach their maxima, the ratio of the integral scale to the Taylor microscale $\lambda = (15/2)^{1/2}u_0\Omega^{-1/2}$ is about 2.5 and the ratio of the Taylor microscale to the

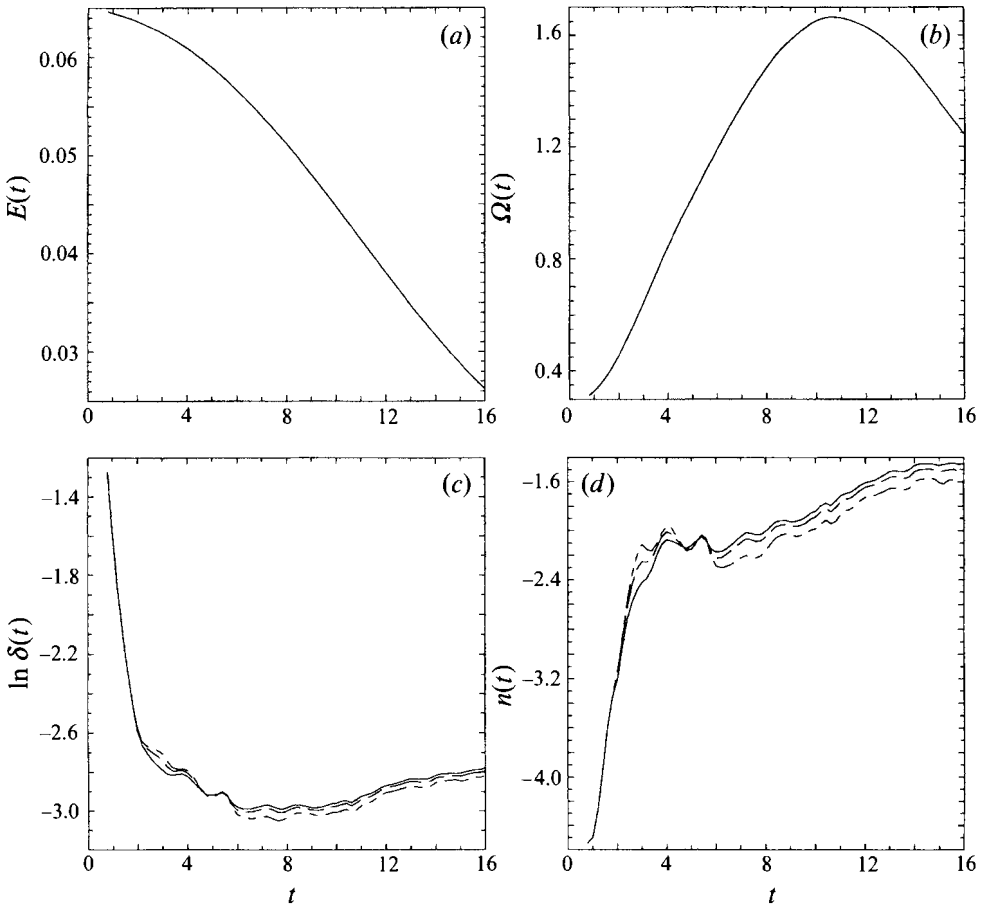

FIGURE 10. Temporal evolution of characteristic quantities for the turbulence numerical simulation of §3. (*a*) Total energy $E(t)$; (*b*) total enstrophy $\Omega(t)$; (*c*) logarithmic decrement $\delta(t)$; (*d*) algebraic prefactor $n(t)$. For curves (*c*) and (*d*), the wavenumber ranges of fit are 5–107 (solid line), 5–117 (long dashed line) and 5–127 (long-short dashed line)

Kolmogorov scale $\eta = 2^{-1/4}\nu^{1/2}\Omega^{-1/4}$ approximatively 15.6. Note that in decaying turbulence, the Kolmogorov scale is not easily interpreted and a better characteristic small scale is provided by the logarithmic decrement $\delta(t)$ which displays several regimes. An early exponential decay associated with the almost inviscid regime, persists up to $t \approx 1.2$. This decay is then slowed down by viscosity, especially after $t = 2$ when the enstrophy approaches its first inflection point. Herring & Kerr (1993) noted that, at this stage, the skewness reached its maximum. Between $t \approx 6$ and $t \approx 9$, $\delta(t)$ is almost constant. Later on, it increases slowly because of the decrease of the Reynolds number. At its minimum, $\delta(t)$ is about twice the mesh size $h = 2\pi/256$, which ensures that the flow is fully resolved during the whole simulation. Although no inertial range is visible by inspection of the energy spectra plotted in figure 11 at times $t = 0.8$, 2.6, 6.8 and 16, the algebraic prefactor $n(t)$ is meaningful. Its behaviour is different from that of the inviscid flow displayed in figure 11(*b*) of Brachet *et al.* (1992). While at zero viscosity, $n(t)$ shows a tendency to saturate at a value close to -4, in the viscous case, it increases rapidly, reaching a value close to -2 at time $t \approx 3$. This value, associated with the presence of vortex layers whose thickness has

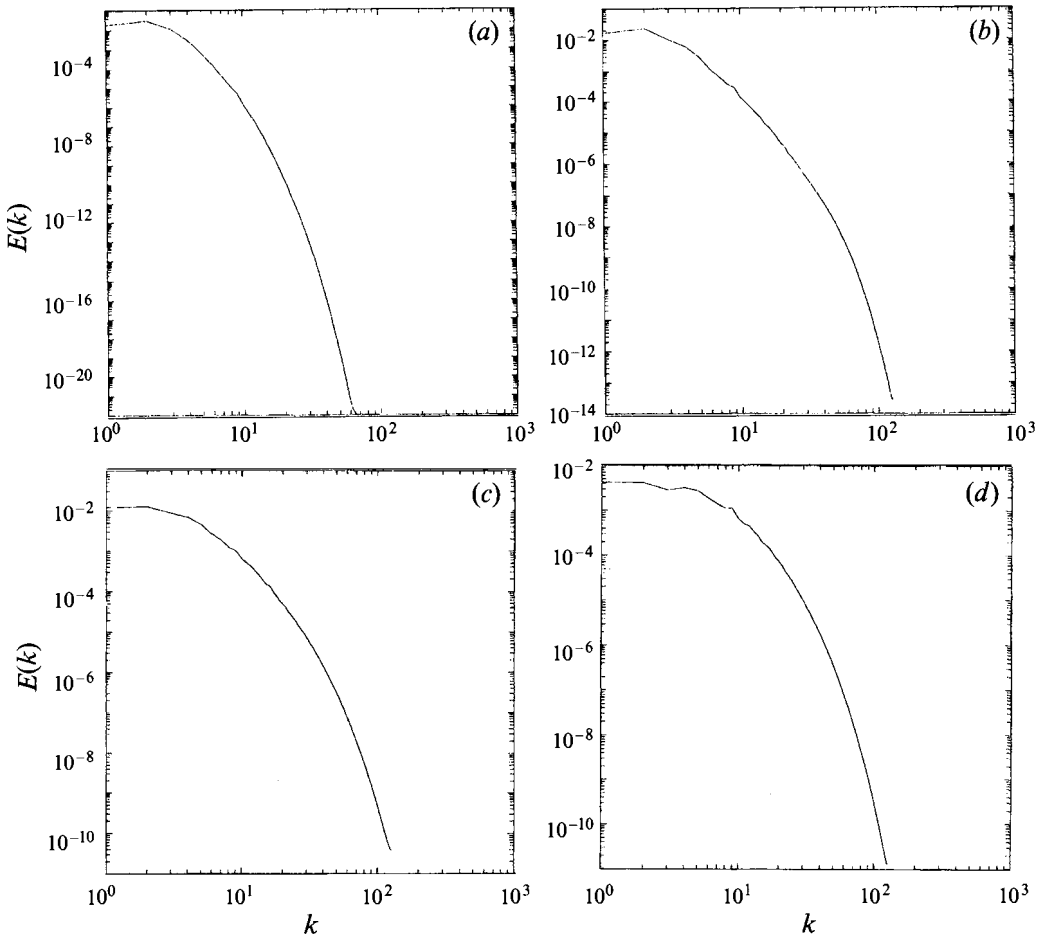

FIGURE 11. Energy spectra at times t=0.8, 2.6, 6.8 and 16(a–d).

saturated under the effect of viscosity, is preserved until $t \approx 6$. Later on, $n(t)$ grows slowly, until $t \approx 14$. Afterwards, it remains mostly constant during several eddy turnover times, at a value between -1.45 and -1.6 depending on the fit range, but always slightly in excess of the Kolmogorov exponent. When the run is interrupted at $t = 16$, almost two thirds of the total energy has been dissipated.

Visualizations in physical space were performed, using the 'Interactive Conic Flight Simulator' of Angilella, Astruc & Vincent (1993). The colour code is chosen such that blue, green, yellow, red and purple correspond to increasing values of the field amplitude. Figure 12 shows snapshots of the vorticity field (within a sub-cube of 45^3 grid points corresponding roughly to the integral scale) about a vortex layer formed by early time shrinking of a vortex blob. Two points of view are presented. Overviews of the structure are shown on the left-hand side and cross-sections on the right-hand side, at times $t = 1.6$, $t = 2$ and $t = 2.6$. We observe a local intensification of the vorticity (by a factor 5) leading to a vortex tube. Furthermore, as seen on the cross-section, the layer rotates and takes a characteristic S-shape. Note in particular the disappearance of the layer near the tube. A similar evolution was observed by Ruetsch & Maxey (1992) in stationary turbulence, using a resolution of 96^3 grid

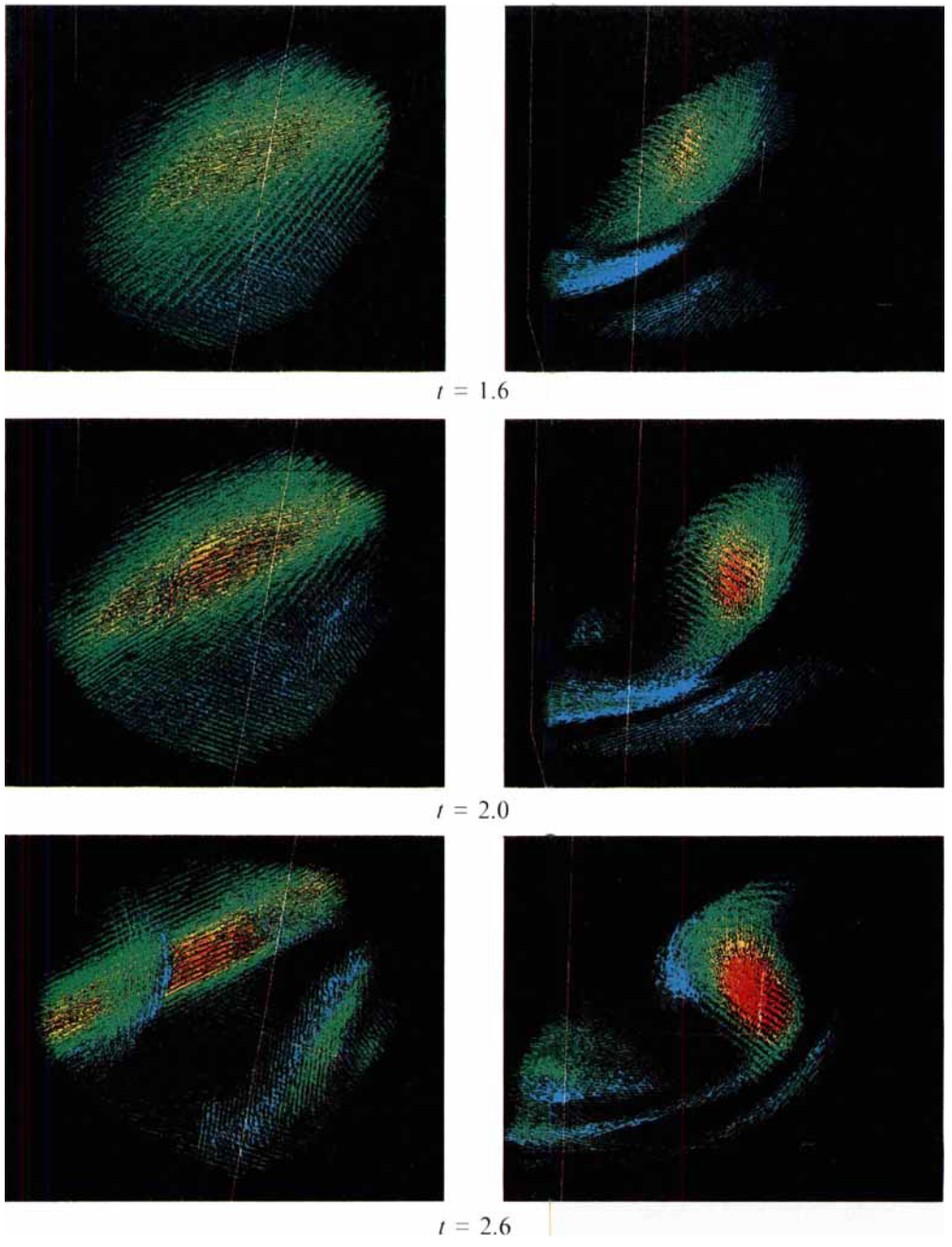

FIGURE 12. Overviews (right-hand side) and cross-sections (left-hand side) of a vortex layer formed at early time. The formation of a vortex tube embedded in the vortex layer is visible.

points (see in particular their figure 9*a*). Figure 13 displays the evolution of three nearby vortex layers which appear later in time. One of them is stable. For the second one, vorticity concentration starts around $t = 3.4$ but is rapidly inhibited and is no longer visible at $t = 4$. At this time, the third vortex layer displays a strong vorticity

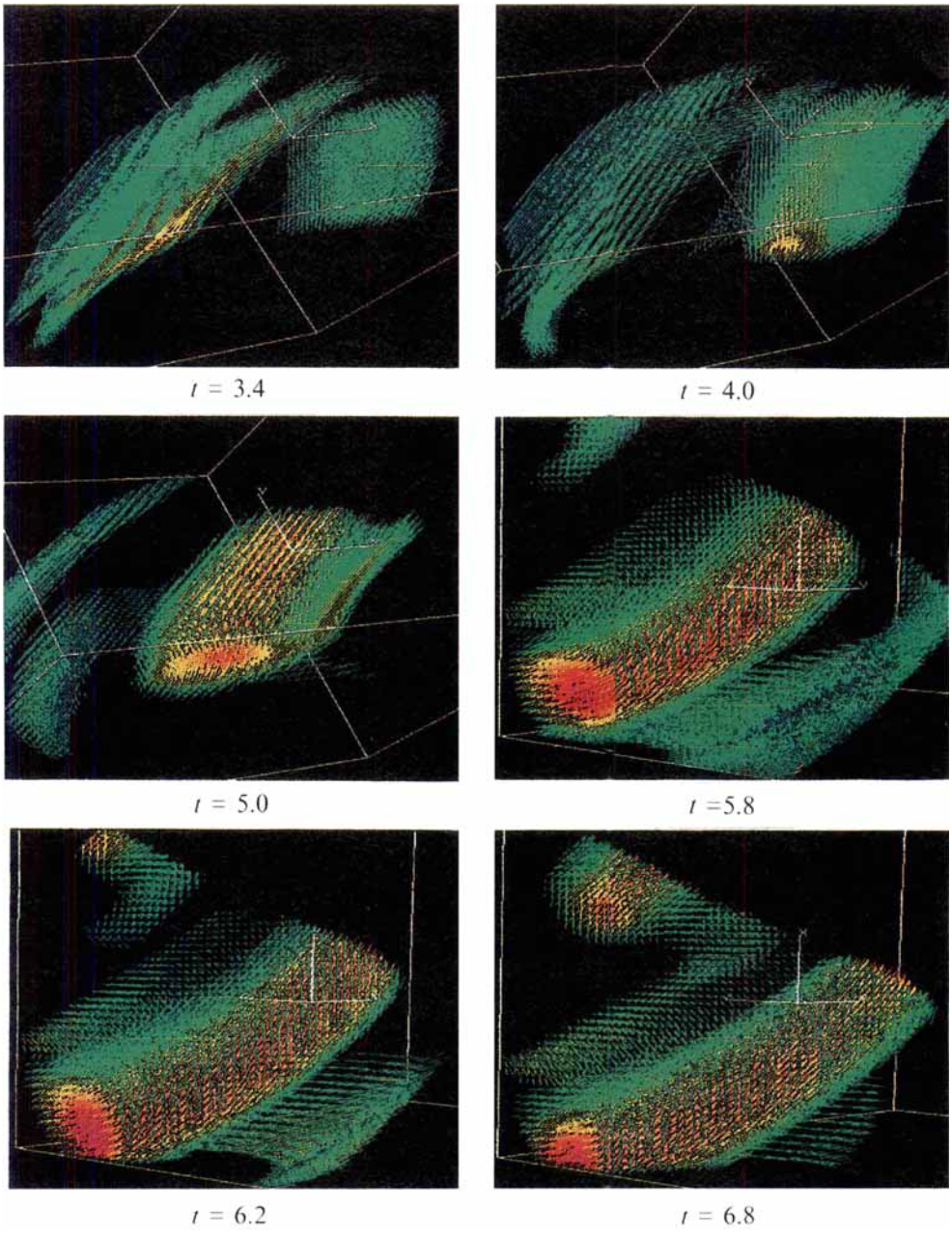

FIGURE 13. Overviews of vortex layer formed at a later time showing vorticity concentration and roll-up of the vortex layer after an intense vortex tube has been formed.

concentration. At $t = 5$, a vortex tube has already been formed. It induces a velocity field which advects the surrounding vortex layers, rolling them around the tube. Such a roll-up of the sheet around a vortex core is reminiscent of the strained spiral vortices considered by Lundgren (1982, 1993). Pictures at later times show the persistence of these dynamics. Here, vorticity concentration corresponds to an amplification by a

factor 3 to 4, comparable to that obtained in the asymptotic model. Note that around $t = 6.2$, a second vortex tube has been formed.

3.2. *Possible mechanisms for vortex tube formation*

From the above observations, we can argue that intense vortex tubes are produced by a concentration of vorticity within vortex layers which significantly roll up only after tubes have been formed. At any given time there is coexistence of both vortex tubes and vortex sheets, the former corresponding to the most intense vorticity structures, the latter being associated with moderate values of the vorticity, but still larger than the r.m.s. amplitude (She *et al.* 1991). As shown numerically by Tanaka & Kida (1993), once tubes have been formed, they can be identified as regions of strong vorticity but moderate strain, while in persistent vortex layers, strain and vorticity are both large. As noted by Kerr (1985), Brachet (1991), Kida & Ohkitani (1992) and Vincent & Meneguzzi (1994), the local dissipation (proportional to the square strain tensor) is especially strong not within the vortex tubes but rather in their neighbourhood. Tubes create regions of important shear at their periphery and, as noticed by Ruetsch & Maxey (1991), this shear is even more intense when strain fields of neighbouring such structures overlap. Although tubes can be viewed as rare events occupying a very small fraction of the total volume, it has been argued, on the basis of a laboratory experiments where polymers are used to inhibit tube formation, that these structures contribute significantly (although indirectly) to energy dissipation when they break down (Bonn *et al.* 1993).

In the context of the model discussed in §2, tube formation is related to the presence of a constant and uniform strain which creates vortex layers and induces vorticity concentration. In order to test this assumption, we display in figure 14 snapshots of regions of intense vorticity (arrows) together with iso-surfaces of the intermediate eigenvalue λ_2 (in blue) of the strain tensor S_{ij}. Since vorticity is aligned with the intermediate eigenvector of the strain tensor, maps of the associated eigenvalue correspond with that of $\omega_i S_{ij} \omega_j$ shown in Ruetsch & Maxey (1992). This eigenvalue λ_2 also corresponds to leading order with the parameter γ introduced in the model of §2. Figure 14 is for a run performed at a resolution of 180^3 grid points and a Reynolds number $Re \approx 250$. The dynamics is very analogous to that presented in §3.1. On the left-hand side of the figure, the iso-surfaces correspond to about 2/3 of the maximum of λ_2 while the ratio is about 1/2 on the right-hand-side figures. Three different times are presented. At the early time, the vortex layer is only weakly perturbed. The eigenvalue λ_2 remains constant along the directions parallel to the vortex layer and varies only slowly in the transverse direction. This configuration is still visible at intermediate time when vorticity begins to concentrate. At the latest time, when the tube is intense, the behaviour of the eignevalue λ_2 has significantly changed. At this time, the asymptotics of the model (which allowed us to identify λ_2 and γ) breaks down. The dynamics can then be described as that of a vortex tube subject to an almost radial uniform strain, as considered by Moffatt, Kida & Ohkitani (1994) in the limit of large Reynolds numbers. These authors showed that the structure of the vortex tube is mostly independent of the strain parameters and that regions of large vorticity and large dissipation do not overlap. These properties could explain the persistence of vortex tubes in turbulent flows.

There is little doubt that formation of vortex sheets in incompressible turbulence requires a local strain. Nevertheless, after a layer has been formed, vorticity concentration can also develop in the absence of an external strain as shown by Baker & Shelley (1990). Indeed, in the strongly nonlinear regime, a finite-width vor-

tex layer, when significantly distorted, generates a strain in the plane of the shear flow associated to the vortex layer. A combination of a transverse compression with the self-induced rotation due to the finite width of the layer produces a converging spanwise velocity, leading to vorticity concentration. The analogy between this process and that discussed in §2 explains the similarity between the observed focusings (figure 12(*b*) of Baker & Shelley 1990 and figures 5 and 7 of the present paper). Nevertheless, the presence of an external strain similar to that of §2 can be inferred from numerical simulations of incompressible turbulence where tubes are seen to lengthen (Vincent & Meneguzzi 1994) for a while after their formation. Furthermore, the strongest tubes, which sometimes reach a significant fraction of the integral scale, usually result from the merging of previously smaller parallel tubes originating from the same shear zone.

Note that in supersonic turbulence, vortex layers can also appear as slip surfaces behind shock interactions with no external strain. Such layers are also observed to form tubes, that are often subject to kink instabilities (Porter, Pouquet & Woodward 1994).

3.3. *Scaling properties of the vortex tubes in fully developed turbulence*

We address here some properties of vortex tubes in stationary high Reynolds number turbulence. The model discussed in §2 involves three quantities, L, σ_0, and γ that have to be related to turbulence characteristics. An important question concerns the scaling of the layer thickness or of the tube diameter δ_0 (which within both the model and the simulations appears to be thicker) with the large-scale Reynolds number Re. Using the Kolmogorov scaling law relating the typical velocity difference u_0 at the integral scale l_0 to the velocity difference σ_0 at the scale L of the layer perturbation, we get $\sigma_0 \approx u_0(L/l_0)^{1/3}$ and $\gamma \approx (u_0/l_0)(L/l_0)^{-2/3}$. It follows that the diameter $\delta_0 = (\nu/\gamma)^{1/2}$ of the resulting tube scales like $l_0 Re^{-1/2}(L/l_0)^{1/3}$. Such a tube will be elongated by the strain, until it reaches a length of order L. For tubes formed in one step from a vortex layer, we thus predict a relation between the length and the diameter, which reproduces qualitatively the observation that in laboratory turbulence, long tubes are thicker than short ones (Cadot, Douady & Couder 1994, where similar scaling arguments have been proposed independently). Taking L to be the Taylor microscale λ_T (the vorticity correlation length), we get $\delta_0 \approx l_0 Re^{-2/3}$, which is larger than the Kolmogorov scale $l_d = l_0 Re^{-3/4}$, obtained when choosing $\sigma_0 \approx u_0$ and $\gamma \approx \omega'$, the enstrophy square root, as suggested by Jiménez *et al.* (1993). Although the Reynolds numbers achieved in the present numerical simulations of turbulence are hardly sufficient to precisely characterize the scaling properties of the transverse dimensions of layers and tubes with Re, the diameters of the tube cores seem to be intermediate between the Taylor microscale and the Kolmogorov scale (Jiménez 1992). Furthermore in a recent paper, Novikov (1993) suggests that the scale relevant for vorticity dynamics is $l_0 Re^{-3/10}$ rather than the Taylor microscale $\lambda_T \approx l_0 Re^{-1/2}$. This leads to an even larger value $\delta_0 \approx l_0 Re^{-3/5}$. Much longer tubes ($L \sim l_0$) with a diameter $\delta \sim 4\eta$ were observed in Jiménez *et al.* (1993). As suggested by Jiménez & Wray (1994), such structures, along which the local strain is observed to change sign on a Taylor microscale, could result from the coalescence of shorter tubes formed previously.

Note that the scaling laws are probably different in the context of freely decaying turbulence. Vortex layers and tubes have in this case a strong memory of the initial conditions and it is then natural to set $\sigma_0 \approx u_0$, $L \approx l_0$ and $\gamma \approx u_0/l_0$. A similar situation also occurs in laboratory turbulence generated by a large-scale shear flow (Douady *et al.* 1991). The tube diameters then approach the Taylor microscale λ_T.

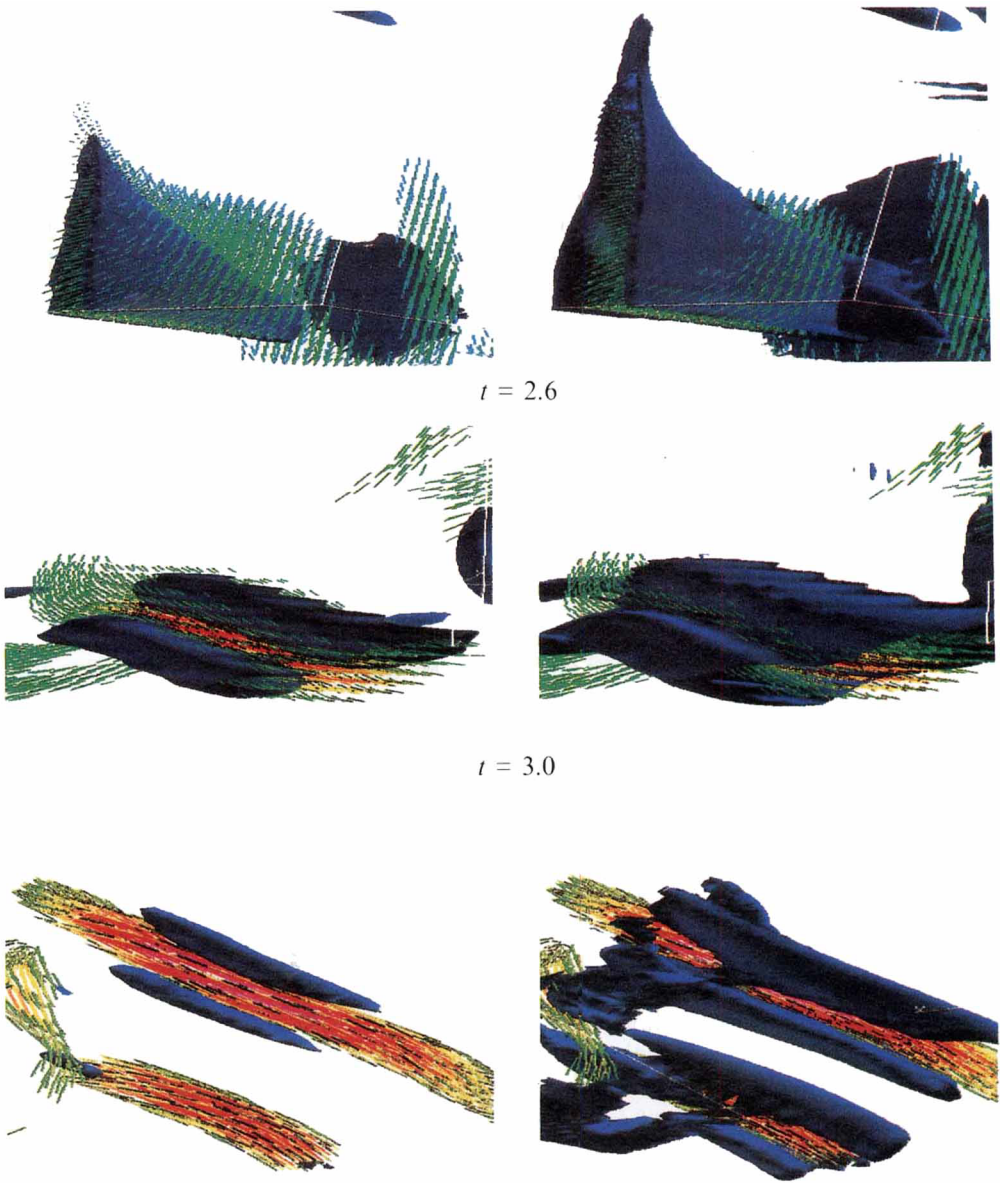

FIGURE 14. Snapshots of vorticity field and iso-surfaces (at about 2/3 and 1/2 of the maximum on the left- and right-hand sides respectively) of the intermediate eigenvalue of the symmetrized velocity gradient matrix at three different times.

Coming back to the case of stationary turbulence and taking $L \approx \lambda_T$, we also obtain $S \approx 1$, $R \approx Re^{1/3}$ and $\zeta \approx \epsilon \approx \mu \approx Re^{-1/6}$. More generally, the Reynolds number μ^{-1} of a tube of length L is expected to scale like $Re^{1/2}(L/l_0)^{2/3}$. The slow variation of μ^{-1} with Re indicates that the turbulence Reynolds number should be very large before tubes can become unstable. As a consequence, in numerical simulations, vortex breakdowns were observed only rarely (Pumir 1994). In contrast, in the experiment performed by Douady *et al.* (1991) where the Reynolds number reaches 80 000, vortex

tubes usually appear as rather straight lines but develop helical distortions similar to kinks, which lead to their disruption. To study the question of tube stability, the basic structure can be the axisymmetric Burgers vortex tubes. When subject to an axisymmetric strain, Burgers vortex tubes are stable against two-dimensional perturbations but their behaviour against three-dimensional perturbations is unknown (Saffman 1992).

3.4. *Spectral signature of vortex tubes*

The presence of vortex tubes should affect the spectral dynamics of homogeneous turbulence. It is easily checked that the Fourier transform of the velocity field $\boldsymbol{v}(\boldsymbol{k})$ created by a (Burgers) vortex tube behaves like $1/k$ as long as the scale k^{-1} is large compared to the tube radius and small compared to its length. The associated energy spectrum (obtained by averaging $\frac{1}{2}|\boldsymbol{v}(\boldsymbol{k})|^2$ on a two-dimensional shell of radius k), thus scales like $1/k$ (Townsend 1951). Such an energy spectrum was observed by Porter, Pouquet & Woodward (1992, 1994) in numerical simulations of compressible turbulence during the late post-supersonic regime, when the compressibility effects are already mild and a great number of vortex tubes are visible in physical space. The computations were done using the so-called Piecewise Parabolic Method (PPM), an algorithm for numerical modelling of the small-scale dissipation which enables one to simulate highly turbulent flows. With a resolution of 256^3 grid points, these authors observed an extended spectral range where the energy spectrum of the solenoidal velocity varies as k^{-1}. With a resolution of 512^3 which can be viewed as corresponding to a higher effective Reynolds number, a $k^{-5/3}$ spectrum develops, followed at larger wavenumbers by a k^{-1} range, the transition occurring close to the Taylor wavenumber. Although the numerical dissipation of the PPM may be significantly different from the molecular dissipation of the Navier–Stokes equations, the global properties of the vortex tubes which are mostly non-dissipative structures, should be preserved by this method. The Reynolds numbers of a few hundreds presently reached in direct numerical simulations of the Navier–Stokes equations are not large enough to make similar observations. However as reported by Jiménez *et al.* (1993), the local energy spectrum in the regions of the flow including vortex tubes display a k^{-1} behaviour, while the global spectrum is consistent with $k^{-5/3}$. In this context, it is noticeable that for several numerical simulations (see figure 10(*d*) and also Vincent & Meneguzzi 1991), precise fits of the (global) energy spectrum in a regime consistent with the Kolmogorov analysis, lead to an exponent slightly shallower than $-5/3$, while most of the predictions for the intermittency corrections to the energy cascade, and also the effect of viscous dissipation would tend to steepen the spectrum. Similar evidence was noticed in the context of laboratory turbulence. By analysing data from Gagne & Castaing (1991) where the Taylor microscale Reynolds number ranges from 130 to 130 000, She & Jackson (1993) obtained an empirical universal fit for the energy spectrum of the form

$$E(k) = E(k_p)\left[\left(\frac{k}{k_p}\right)^{-5/3} + 0.8\left(\frac{k}{k_p}\right)^{-1}\right] \mathrm{e}^{-\mu k/k_p}, \tag{3.1}$$

where k_p is defined as the peak wavenumber for the dissipation spectrum $k^2E(k)$. Figure 2 of She & Jackson (1993) clearly shows that deviation from Kolmogorov $k^{-5/3}$ spectrum occurs at wavenumbers clearly smaller than k_p (roughly by a factor five). If, as suggested by the model, the energy transfer in this range results from vorticity concentration into tubes within vortex layers, as a consequence of a large-scale

instability, it should be viewed as non-local. The question arises of the asymptotic behaviour of this range if, as expected, vortex tubes become unstable when the Reynolds number becomes large enough.

4. Summary

We have presented an asymptotic analysis for the nonlinear dynamics of a vortex layer subject to an external plane strain. This approach leads to a system of partial differential equations in one space variable for the strength, the distortion and the thickness of the layer. Their numerical integration shows that vorticity concentrates into stationary structures corresponding to vortex tubes. We also displayed detailed visualizations of regions of intense vorticity in numerical simulations of freely decaying turbulence. Sophisticated three-dimensional graphic software led us to a precise description of the small-scale dynamics which suggests that vortex tubes observed in incompressible homogeneous turbulence result from concentration within a vortex layer formed at earlier time. A detailed investigation shows that both vorticity and total strain are satisfactorily reproduced by the asymptotic model. Layer roll-up is also visible in numerical simulations, but this is mainly a secondary process, corresponding to a vortex layer wrapping around an intense vortex core.

Our model remains valid at large Reynolds numbers. It predicts that, in this regime, the diameters of the vortex tubes should significantly exceed the Kolmogorov scale. In a slightly modified form, the model can address the inviscid limit leading to the conclusion that viscosity, which prescribes a finite thickness for the vortex layers, is an essential ingredient for vortex tube formation. In fact the tubes probably become unstable at large enough Reynolds numbers as suggested by laboratory experiments of Douady *et al.* (1991) where helical instabilities yielding tube disruptions are observed. Development of such helical instabilities may contribute to a significant stirring of the flow at much larger scales.

We thank Y. Couder, Y. Gagne, J. Jiménez, H. K. Moffatt and the referees for useful discussions and comments. Turbulence numerical simulations were performed on the CRAY2 of the Centre de Calcul Vectoriel pour la Recherche (Palaiseau) and post-processing on the CRAY C98 of the Institut du Développement et des Ressources Informatiques Scientifiques (Orsay). The asymptotic model was solved on the CRAY-YMP of the Institut Méditerranéen de Technologie (Marseille) thanks to computer time provided by the Région Provence Côte d'Azur. This work benefited from support from the CNRS through the Groupe de Recherche "Mécanique des Fluides Numérique".

REFERENCES

ANGILELLA, J. R., ASTRUC, D. & VINCENT, A. 1993 The cone of vision: a new technique for an interactive volumetric display. *ACM Transaction on Graphics* (submitted).

ASHURST, W. T., KERSTEIN, A. R., KERR, R. M. & GIBSON, C. H. 1987 Alignment of vorticity and scalar gradient with strain rate in simulated Navier-Stokes turbulence. *Phys. Fluids* **30**, 2343–2353.

BAKER, G. R. & SHELLEY, M. J. 1990 On the connection between thin vortex layers and vortex sheets. *J. Fluid Mech.* **215**, 161–194.

BETCHOV, R. 1956 An inequality concerning the production of vorticity in isotropic turbulence. *J. Fluid Mech.* **1**, 497–504.

BONN, D., COUDER, Y., DAM, P. H. J. VAN & DOUADY, S. 1993 From small scales to large scales in three-dimensional turbulence: The effect of diluted polymers. *Phys. Rev.* E **47**, R28–R31.

BRACHET, M. E. 1991 Direct simulation of three-dimensional turbulence in the Taylor-Green vortex. *Fluid Dyn. Res.* **8**, 1–8.

BRACHET, M. E., MENEGUZZI, M., VINCENT, A., POLITANO, H. & SULEM, P. L. 1992 Numerical existence of smooth self-similar dynamics and possibility of subsequent collapse for three-dimensional ideal flows. *Phys. Fluids* A **4**, 2845–2854.

CADOT, O., DOUADY, S. & COUDER, Y. 1994 Characterisation of the low pressure filaments in a 3D turbulent shear flow. *Phys. Fluids* (to appear).

CHANDRASEKHAR, S. 1961 *Hydrodynamic and Hydromagnetic Stability.* Oxford University Press.

DOUADY, S., COUDER,Y. & BRACHET, M. E. 1991 Direct observation of the intermittency of intense vorticity filaments in turbulence. *Phys. Rev. Lett.* **67**, 982–986.

GAGNE, Y. & CASTAING, B. 1991 Une représentation universelle sans invariance globale d'echelle des spectres d'energie en turbulence développée. *C.R. Acad. Sci. Paris* **312**, 441–445.

HERRING, J. R. & KERR, R. M. 1993 Development of enstrophy and spectra in numerical turbulence. *Phys. Fluids* A **5**, 2792–2798.

JIMÉNEZ, J. 1992 Kinematic alignment effects in turbulent flows. *Phys. Fluids* A **4**, 652-654.

JIMÉNEZ, J. & WRAY, A. A. 1994 Intense vortices in isotropic turbulence. *Proc. Fifth European Turbulence Conference, Siena, July 1994*, to appear.

JIMÉNEZ, J., WRAY, A. A., SAFFMAN, P. G. & ROGALLO, R. S. 1993 The structure of intense vorticity in isotropic turbulence. *J. Fluid Mech.* **255**, 65–90.

KERR, R. M. 1985 Higher-order derivative conclusions and the alignment of small-scale structures in isotrophic numerical turbulence. *J. Fluid Mech.* **153**, 31–58.

KIDA, S. & OHKITANI, K. 1992 Spatio-temporal intermittency and instability of a forced turbulence. *Phys. Fluids* A **4**, 1018–1027.

LIN, S. J. & CORCOS, G. M. 1984 The mixing layer: deterministic models of a turbulent flow. Part 3. The effect of plane strain on the dynamics of streamwise vortices. *J. Fluid Mech.* **141**, 139–178.

LUNDGREN, T. S. 1982 Strained spiral vortex model for turbulent fine structure. *Phys. Fluids* **25**, 2193-2203.

LUNDGREN, T. S. 1993 A small scale turbulent model. *Phys. Fluids* A **5**, 1472-1483.

MAJDA, A. 1986 Vorticity and the mathematical theory of incompressible fluid flow. *Commun. Pure Appl. Maths* **39**, S187–S220.

MEIRON, D. I., BAKER, G. R. & ORSZAG, S. A. 1982 Analytic structure of vortex sheet dynamics. Part 1. Kelvin–Helmoltz instability. *J. Fluid Mech.* **114**, 283–298.

MOFFATT, H. K., KIDA, S. & OHKITANI, K. 1994 Stretched vortices - the sinews of turbulence; large Reynolds number asymptotics. *J. Fluid Mech.* **259**, 241–264.

NEU, J. C. 1984 The dynamics of stretched vortices. *J. Fluid Mech.* **143**, 253–276.

NOVIKOV, E. A. 1993 Statistical balance of vorticity and a new scale for vortical structures in turbulence. *Phys. Rev. Lett.* **71**, 2718–2720.

PALAIS, B. 1988 Blowup for nonlinear equations using a comparison principle in Fourier space. *Commun. Pure Appl. Maths* **41**, 165–196.

PORTER, D. H., POUQUET, A. & WOODWARD, R. P. 1992 Three-dimensional supersonic homogeneous turbulence: a numerical study. *Phys. Rev. Lett.* **68**, 3156–3159.

PORTER, D. H., POUQUET, A. & WOODWARD, R. P. 1994 Kolmogorov-like spectra in decaying three-dimensional supersonic turbulence. *Phys. Fluids* **6**, 2133–2142.

PUMIR, A. 1994 A numerical study of pressure fluctuations in three-dimensional, incompressible, homogeneous, isotropic turbulence. *Phys. Fluids* **6**, 2071–2083.

RUETSCH, G. R. & MAXEY, M. R. 1991 Small-scale features of vorticity and passive scalar fields in homogeneous isotropic turbulence. *Phys. Fluids* A **3**, 1587–1597.

RUETSCH, G. R. & MAXEY, M. R. 1992 The evolution of small-scale structures in homogeneous isotropic turbulence. *Phys. Fluids* A **4**, 2747–2760.

SAFFMAN, P. G. 1992 *Vortex Dynamics.* Cambridge University Press.

SHE, Z. S. & JACKSON, E. 1993 On the universal form of energy spectra in fully developed turbulence. *Phys. Fluids* A **5**, 1526–1528.

SHE, Z. S., JACKSON, E. & ORSZAG, S. A. 1990 Intermittent vortex structures in homogeneous isotropic turbulence. *Nature* **344**, 226–228.

SHE, Z. S., JACKSON, E. & ORSZAG, S. A. 1991 Structure and dynamics of homogeneous turbulence: Models and simulations. *Proc R. Soc. Lond.* A **434**, 101–124.

SIGGIA, E. D. 1981 Numerical study of small-scale intermittency in three-dimensional turbulence. *J. Fluid Mech.* **107**, 375–406.

SULEM, C., SULEM, P. L. & FRISCH, H. 1983 Tracing complex singularities with spectral methods. *J. Comput. Phys.* **50**, 138–161.

TANAKA, M. & KIDA, S. 1993 Characterisation of vortex tubes and sheets. *Phys. Fluids* A **5**, 2079–2082.

TOWNSEND, A. A. 1951 On the fine scale structure of turbulence. *Proc. R. Soc. Lond.* A **208**, 534–542.

VINCENT, A. & MENEGUZZI, M. 1991 The spatial structure and statistical properties of homogeneous turbulence. *J. Fluid Mech.* **225**, 1–20.

VINCENT, A. & MENEGUZZI, M. 1994 On the dynamics of vorticity tubes in homogeneous turbulence. *J. Fluid Mech.* **258**, 245–254.